Synthesis of hierarchical NiS microflowers for high performance asymmertric supercapacitor

Bing Guan, Yu Li, Biyue Yin, Kefan Liu, Dawei Wang, Huaihao Zhang, Changjing Cheng

PII: S1385-8947(16)31417-6
DOI: http://dx.doi.org/10.1016/j.cej.2016.10.016
Reference: CEJ 15871

To appear in: *Chemical Engineering Journal*

Received Date: 11 August 2016
Revised Date: 3 October 2016
Accepted Date: 4 October 2016

Please cite this article as: B. Guan, Y. Li, B. Yin, K. Liu, D. Wang, H. Zhang, C. Cheng, Synthesis of hierarchical NiS microflowers for high performance asymmertric supercapacitor, *Chemical Engineering Journal* (2016), doi: http://dx.doi.org/10.1016/j.cej.2016.10.016

Synthesis of hierarchical NiS microflowers for high performance asymmertric supercapacitor

Bing Guan [a], Yu Li [a], Biyue Yin [a], Kefan Liu [a], Dawei Wang [a], Huaihao Zhang [a,*], and Changjing Cheng [b,*]

[a] College of Chemistry and Chemical Engineering, Yangzhou University, Yangzhou 225002, PR China

[b] College of Chemistry & Environment Protection Engineering, Southwest University for Nationalities, Chengdu, 610041, China

Abstract: In this work, the hierarchical NiS microflowers were synthesized using $Ni(OH)_2$ as precursors through sulfuration process. The microstructure and chemical composition of as-prepared NiS was confirmed by means of SEM, TEM, XRD, BET and XPS. The SEM analysis results demonstrated that the NiS microflowers were composed of hierarchical nanoplates, and its surface was much rougher compared to that of $Ni(OH)_2$ templates after sulfidation. Electrochemical characterization revealed that NiS presented high specific capacitance in 3 M KOH electrolyte (1122.7 $F \cdot g^{-1}$ at current density of 1 $A \cdot g^{-1}$) and good electrochemical cycling stability (97.8% of the specific capacitance is retained after 1000 charge-discharge cycles at current density of 10 $A \cdot g^{-1}$). Furthermore, an asymmetric supercapacitor, NiS as the positive electrode and activated carbon as the negative electrode, delivered high energy density of 31 $Wh \cdot kg^{-1}$ at power density of 0.9 $kW \cdot kg^{-1}$ under operating voltage window of 1.8 V.

Keywords: Microflowers; NiS; Asymmetric supercapacitor; Energy density

[*]corresponding author. Tel/Fax: +86 51487975244

E-mail address: huaihaozhang@163.com(H.H. Zhang); chengcj@swun.edu.cn(C.J.C)

1. Introduction

Supercapacitors (SCs), also electrochemical capacitors, have received intense attention because of their higher power density than secondary batteries and higher energy density than conventional dielectric capacitors. These superior advantages enable them promising in various areas, such as portable electronic devices, hybrid electric vehicles, and back-up power supplies [1-4]. Based on the charge storage mechanism, SCs can be typically classified into electrical double-layer capacitor (EDLCs) and pseudocapacitors. EDLCs build up an electrical charge at the electrode-electrolyte interface, whereas pseudocapacitors based on the fast, reversible redox reaction take place on or near the surface of electroactive material [5-9]. EDLCs based on carbonaceous materials, such as activated carbon, carbon nanotubes and graphene, etc. The carbon materials have high electric conductivity and long life cycle, but they usually suffer from the small double-layer capacitance. Alternatively, pseudocapacitors use transition metal oxides/hydroxides as well as conducting polymers as the electroactive materials such as RuO_2, MnO_2, $Ni(OH)_2$ and PANI, etc. Compared with EDLCs, pseudocapacitors could provide higher specific capacitance (C_m), attributing to the fast and reversible redox reaction on the surface of electroactive materials [10-12]. Among the numerous transition metal oxides, RuO_2 exhibits tremendous application potentiality as a promising electroactive material due to its high theoretical specific capacitance, good electric conductivity and long cycle lifetime. However, its resource scarcity, high cost and toxic nature limits its widely commercial application [13]. Hence, much effort has been focused on alternative

electrode materials with low price, environmentally friendly and good capacitive performance such as MnO_2 [14], NiO [15], Co_3O_4 [16], $MnCo_2O_{4.5}$ [17] and V_2O_5 [18] and so forth. Nonetheless the conductivity of transition metal oxides is too low to favor rapid electron transport at high rate capability, which limits its extensive application in practice [19].

Recently, transition metal sulfides such as FeS_2, CuS, MoS_2, NiS_2 and CoS_2 possess promising application future in areas of hydrogen evolution reaction catalysts, sensors, solar cells, lithium ion batteries and SCs due to their unique optical and electrical properties [20-28]. Compared with corresponding oxides, transition metal sulfides have higher conductivity, mechanical and thermal stability and richer redox reactions. Therefore, they have better capacitance performance and potential to be applied to electroactive materials for SCs [29-34]. As one of the important class of transition metal chalcogenides, nickel sulfides exist various phases, such as NiS, NiS_2, Ni_3S_2, Ni_7S_6 and Ni_9S_8. Among them, NiS receives more attention owing to its excellent capacitance performance, high redox activity, safety and low price, which are expected to satisfy the increasing needs of energy storage systems [35-41].

As is known, the morphology and structure of electroactive materials have a key influence on electrochemical behaviors. Thus many researchers desire to develop distinctive morphological NiS in order to design electrode materials with large surface and rough surface to improve the wettability of active materials and short diffusion paths for electrolyte and charge transports [42,43]. A comparison of C_m of NiS microflowers with other forms of NiS, as can be indexed in Table 1. Nevertheless, as

for the synthesis process of samples, the usage of expensive organic solvent and template is unfavorable to its widely application in practice.

Herein, we report a facile sacrificial template method to synthesis hierarchical NiS microflowers—sulfidizing $Ni(OH)_2$ precursor with thiourea in absolute ethanol. The hierarchical structure with high specific surface area can improve the density of active sites, and enhanced the electron transferring and ion diffusing rate, respectively [47]. When applied as the electroactive materials for SCs, the hierarchical NiS microflowers electrodes show a high C_m of 1122.7 $F \cdot g^{-1}$ at 1 $A \cdot g^{-1}$, good cycling stability and rate capability. Furthermore, in order to evaluate the practical application of NiS, an asymmetric supercapacitor, NiS as the positive electrode and activated carbon (AC) as the negative electrode, was assembled (named as NiS//AC). The NiS//AC has extended the operating voltage to 1.8 V in 3 M KOH electrolyte, and achieved energy density of 31 $Wh \cdot kg^{-1}$ with a power density of 0.9 $kW \cdot kg^{-1}$. Meanwhile, the NiS//AC shows a superior cycling and coulombic efficiency. This study reveals the hierarchical NiS microflowers are a promising candidate for high performance SCs.

2. Experimental

2.1. Synthesis of $Ni(OH)_2$ precursors

The synthesis of hierarchical NiS microflowers is depicted in Fig. 1. Typically, 0.872 g of $Ni(NO_3)_2 \cdot 6H_2O$ and 0.364 g of urea were dissolved in 40 mL of deionized water to obtain a pale green solution under vigorous stirring. Then 0.012g trisodium citrate was added to the resulting dispersion. After stirring for 30 min, the resulting

solution was transferred in to a 50 mL Teflon-lined stainless autoclave and kept 150 °C for 24 h. Finally, the autocalve was cooled to room temperature naturally. The green precipitates were collected and washed with deionized water and absolute ethanol several times by centrifugation, and then dried at 60 °C for 8 h.

2.2. Synthesis of hierarchical NiS microflowers

For the formation of NiS microflowers, 0.106 g of the as-obtained precursor was dispersed in to 40 mL of absolute ethanol, followed by addition of 0.228 g of thiourea. After thorough stirring for 5 min, the mixed solution was transferred in to a 50 mL Teflon-lined stainless autoclave and heated at 120 °C for 24 h, and then cooled down to room temperature naturally. The black precipitates were collected by centrifugation, washed with deionized water and absolute ethanol several times, and dried under 60 °C for 8 h. The productivity of the NiS microflowers is 93.64%.

2.3. Materials characterization

The crystallographic information of the as-prepared samples was characterized by X-ray diffraction (XRD, Bruker, D8 Advance, Germany) with Cu K_{α} radiation (λ=1.5406 Å). Chemical valence states and elemental composition of the samples were analyzed by X-ray photoelectron spectroscopy (XPS, Thermo Science, ESCALAB 250Xi, USA). Morphology and structure were analyzed by scanning electron microscopy (FESEM, Hitachi, S-4800 Ⅱ, Japan) equipped with an energy-dispersive X-ray spectroscopy detector (EDS), transmission electron microscopy (TEM, Philips, TECNAI12, Holland) and high resolution transmission electron microscope (HRTEM, FEI, TECNAI G2F30 S-TWIN, USA). The surface

areas and the pore-size distribution were measured on N_2 adsorption analyzer (Micromeritics, TriStar 3000, USA).

2.4. Electrochemical measurements

Electrochemical tests of as-obtained samples were performed in a three-electrode mode in 3 M KOH solution, the Ag/AgCl and platinum plate as the reference and counter electrodes, respectively. The working electrode was prepared by mixing the active material, conductive graphite and polytetrafluoroethylene (PTFE) in a mass ratio of 80:15:5. A proper amount of absolute ethanol was then added to the mixture to promote homogeneity. The slurry mixture was smeared into the Ni foam substrate (1×1 cm^2), dried at 60 °C for 12 h to remove the absolute ethanol fully, and then pressed into a thin foil at a pressure of 10 MPa. The active material mass of a single electrode is about 2~2.5 mg.

The NiS//AC was fabricated based on NiS positive electrode and active carbon (AC) negative electrode. Preparation method of positive and negative electrode was same. The NiS//AC was separated with a glass fiber filter paper, and performed in a two-electrode system in 3 M KOH electrolyte. As for NiS//AC, the charge balance between the two electrodes follow the relationship: $Q_+ = Q_-$. The charge storage by each electrode relates to the C_m, the potential range for discharge process (ΔE) and the mass of the electrode (m) following the equation [34]:

$$Q = C_m \times \Delta E \times m \qquad (1)$$

In order to get $Q_+ = Q_-$, mass balancing will be calculated as following:

$$m_+ / m_- = C_m \times \Delta E_- / C_{m+} \times \Delta E_+ \qquad (2)$$

On the basis of C_m values and potential windows as for NiS and AC, the optimal mass ratio between the two electrodes should be m (NiS)/m (AC) = 0.44.

Cycling voltammetry (CV) and galvanostatic charge-discharge (GCD) were measured on CHI660E electrochemical workstation. Electrochemical impedance spectroscopy (EIS) was conducted on Autolab-PGSTAT in the frequency range between 100 kHz and 0.01 Hz.

3. Resulting and discussion

3.1. Morphology and structure

Fig. 2A shows the XRD patterns of the precursor and NiS. The main characteristic peaks at 12.3°, 24.4°, 34.4° and 59.9° respectively match well with (003), (006), (012) and (110) planes of the $Ni(OH)_2 \cdot 0.75H_2O$ phase (PDF: 38-0715). After vulcanization reaction of precursor, the characteristic peaks of samples transfers to 30.3°, 34.8°, 46.2°, 53.7° and 73.6°, corresponding to the (100), (101), (102), (110) and (202) planes of the NiS phase (PDF: 02-1280), which agree well with the HRTEM. In addition, no impurities peaks are seen in XRD patterns, suggesting high purity of obtained of NiS. And the sharp and narrow characteristic peaks imply the NiS has high crystallinity. EDS spectrum (Fig. S1) further demonstrates that NiS is mainly composed of Ni and S, and the ratio of Ni and S (the inset in Fig. S1) is determined to be about 10:11, which is close to the formula of NiS.

From Fig. 2B and Fig. S2A, N_2 adsorption-desorption isotherm of NiS and precursor ($Ni(OH)_2$), there is a distinct hysteresis loop at a relative pressure of 0.5~1.0, indicating NiS and precursor display type-IV isotherm with a characteristic H3

hysteresis loop associated with mesoporous structure and broad pore-size distribution [50]. The Brunauer-Emmett-Teller (BET) surface area of NiS and precursor are 26.3 $m^2 \cdot g^{-1}$ and 175.2 $m^2 \cdot g^{-1}$, respectively. The BET surface area of NiS appeared decreased compared with the precursor according to the reported literature [9]. The corresponding pore size distribution plot of NiS and precursor are shown in Fig. 2C calculated from adsorption isotherms. It can be clearly seen that the pore size of NiS mainly distributed within the range of 2.07~18.23 nm, while the pore size of precursor (Fig. S2B) was mostly above 2.07 nm from the Barrett-Joyner-Halenda (BJH) method. NiS has a wide pore size distribution and its large dimensional mesoporous is relatively more, corresponding to the obvious hysteresis loop. From Fig. 2C, some large pores are observed due to the stacking nanosheet structure of NiS. The NiS microflower structure provides a large specific surface area and high porosity, facilitate the electrolyte penetration and electrons transfer, and thus improve the capacitive performance [51].

To gain information on the chemical states of NiS, XPS measurements were carried out and the results are shown in Fig. 2(D~F). From Fig. 2D, the survey spectrum of NiS, the peaks at 168.7 and 856.2 eV correspond to S 2p and Ni 2p, respectively. In addition, the C and O elements also occur in survey spectrum, attributing to NiS the exposure to air. The Ni 2p and S 2p spectra were fitted by the Gaussian fitting method, shown in Fig. 2E. The Ni 2p spectrum can be fitted with two spin-orbit doublets and two shark-up satellites. The binding energy at 853.2 and 870.5 eV correspond to the Ni^{2+}, and the binding energy of 855.9 and 873.8 eV is the

characteristic of Ni^{3+} [35,45]. The results showed that Ni existed in two kinds of valence, offering rich redox reactions of NiS. For S 2p spectrum of NiS (Fig. 2F), the binging energy at 161.4 eV suggests that the S element exist as S^{2-}, and the peaks of S $2p_{1/2}$ at 162.5 eV can be owed to sulphur ion in low coordination at NiS surface [52]. Meanwhile, the peak at 168.6 eV could be attributed to sulfur oxides at surface [28].

Fig. 3A and 3B show SEM images of precursor at different magnifications. As shown in Fig. 3A, the precursor showed the microflower structure, mainly comprised of numerous nanosheets with smooth surface (Fig. 3B). Fig. 3C and 3D depict SEM images of NiS. After sulfidation reaction in absolute ethanol, the NiS samples maintain the microflower structure of the precursor (Fig. 3C) and its surface becomes much rougher compared to that of precursor (Fig. 3D). These coarse surfaces not only provide high specific surface areas, but also improve the wettability of active materials for better electron and electrolyte transmission [48]. TEM images (Fig. 3E) clearly reveal that precursor possesses a microflower structure composed of hierarchical nanosheets (Fig. 3F), consistent with SEM results. The hierarchical nanosheet structure can facilitate the access of electrolytes; meanwhile, it is also favorable for structural stability of active materials under repeated GCD process [49]. In agreement with SEM (Fig. 3C and 3D), TEM results further comfirm microflower structure of as-obtained NiS (Fig. 3G). Through red areas comparison of Fig. 3F and 3H, the transparency of the precursor is obviously superior NiS, further demonstrating that NiS has rough surface, which is similar to the SEM result in Fig. 3D. A typical HRTEM image of NiS is presented in Fig. 3I.

The lattice fringes show the characteristics of NiS, in which the interplanar distance of 0.171, 0.258 and 0.296 nm corresponds to the (110), (101) and (100) plane of NiS. Moreover, orderly lattice fringes reveal the well-crystalline of NiS samples.

3.2. Electrochemical performance

The electrochemical measurements of as-obtained samples as an electroactive material were performed. Fig. 4A depicts the CV curves of NiS electrode in a potential range from -0.1~0.6 V at various scan rates from 5 $mV \cdot s^{-1}$ to 100 $mV \cdot s^{-1}$. Obviously, a set of redox peaks is observed, showing typical pseudocapacitive characteristic of NiS. The Faradaic redox of NiS in 3 M KOH electrolyte is shown formula [40]:

$$NiS + OH^- \leftrightarrow NiOH + e^- \quad (3)$$

Notably, CV shapes for NiS has not obvious changes as the scan rate increases, implying its fast charge/discharge capabilities, which is particularly important to power device [46]. In addition, as the scan rate increases, the oxidation and reduction peaks moved to the right and left respectively due to polarization of the NiS [27]. Fig. S3A presents the CV curves of precursor at different scan rates. Apparently, a couple of redox peaks is visible and the redox peaks are almost symmetric with various scan rates, reflecting excellent electrochemical reversibility of precursor electrode.

Fig. 4B shows the GCD curves at different current densities within the potential range of 0~0.45 V. Consistent with the redox peak position in the CV curves, the plateaus in GCD curves indicate NiS electrodes exhibit pseudocapacitive behavior. Furthermore, GCD curves at various current densities are highly symmetrical,

revealing outstanding electrochemical reversibility. The GCD curves of precursor at different current densities are nearly symmetrical (Fig. S3B), implying the good reversibility of redox reaction.

The C_m of NiS and precursor electrodes was calculated by the following equation:

$$C_m = I \times \Delta t / (m \times \Delta V) \qquad (4)$$

Where C_m is the specific capacitance ($F \cdot g^{-1}$), I is the discharge current (A), Δt is the discharge time (s), m is the mass of the active material (g) and ΔV is the potential window during discharge (V). The C_m of NiS and precursor were plotted at different current densities in Fig. 4C. It can be seen that the C_m of NiS evaluated from the discharge curves are 1122.7, 991.6, 913.2, 820.7, 680.3, 465.3 and 323.5 $F \cdot g^{-1}$ at the current densities of 1, 2, 3, 5, 10, 20 and 30 $A \cdot g^{-1}$. Meanwhile, under the same condition of current densities, the C_m of precursor are 686.3, 612.1, 548.3, 465.3, 306.7, 154.1 and 96 $F \cdot g^{-1}$, respectively. Even at a high current density of 30 $A \cdot g^{-1}$, NiS and precursor electrodes still remained about 28.9% and 13.9% of the highest C_m. This can be ascribed to the microflower structure with high specific surface area, which is beneficial for the fast transfer of electrons, leading to high specific capacitance and good rate performance. Moreover, the NiS has higher C_m and better rate performance than precursor.

The comparison of CV curves for NiS and precursor at a scan rate of 5 $mV \cdot s^{-1}$ are shown in Fig. 4D. Apparently, the NiS reveals a larger CV integrated area and higher current density in comparison with that of precursor, suggesting that NiS

electrode exhibits much better pseudocapacitive performance and electrochemical reversibility. The excellent electrochemical performance of NiS may be ascribed to the following factors. First, the high surface area of NiS microflowers could improve the surface wetting of the electroactive materials, providing rich electroactive sites. Second, the porous and open structure of NiS microflowers can short diffusion paths for electrons and ions thus enhance the electrochemical kinetics. Finally, the open space of NiS microflowers can act as the robust reservoir for electrolyte ions, supplying sufficient redox reactions for energy storage [38]. GCD curves of NiS and precursor in a potential window of 0~0.45 V at a current density of 1 $A \cdot g^{-1}$ are presented in Fig. 4E. It can be observed that the symmetry and charge/discharge time of NiS is superior to the precursor, revealing excellent electrochemical reversibility and capacitive behavior for NiS samples.

Nyquist plots of NiS and precursor in the frequency range of 10^{-2}~10^{5} Hz are shown in Fig. 4F. And the equivalent used to fit the impedance curves is also presented (insets in Fig. 4F), which consists of the equivalent series resistance R_s (including the total resistance of ionic resistance of electrolyte, the bluck resistance and the resistance at the interface of the electrolyte/electrode), Warburg impedance W, charge-transfer R_{ct}, double-layer capacitance C_d and Faradaic pseudocapacitor C_F. Nyquist plots have an inconspicuous arc in the high frequency region and a straight line in the low frequency region. Here, the R_s is calculated based on the semicircle intersect on the real axis. It can be observed that the R_s of NiS and precursor are 0.18 and 0.24 Ω respectively, which indicate the higher conductivity of NiS compared to

precursor. Meanwhile, the diameters of semicircles correspond to the R_{ct}, caused by Faradic reactions. The relatively low value of R_{ct} indicates faster electron transport. As indicated in Fig. 4F, the R_{ct} values, calculated by ZSimpWin software, of NiS (2.99 Ω) is smaller than that of precursor (6.31 Ω), indicating that the charge transfer ability of NiS is superior to precursor [45]. The straight lines in the low frequency region describe the diffusion resistance of ion from the electrolyte solution to the electrode interface. Both the straight lines of NiS and precursor in the Nyquist plots inclined at an angle more than 45º, manifesting that the microflower structure can facilitate electrolyte ions transport and more ideal capacitor behavior [53].

The long-term cycling stability is investigated via consecutive GCD tests at a current density of 10 $A \cdot g^{-1}$ for 1000 cycles (Fig. 4G). The C_m of NiS and precursor maintain about 97.8% and 119.7% of their initial value after 1000 cycles. It can be observed that the C_m of NiS and precursor increase firstly, dropped slightly and finally tend to a stable value. In the initial stage, the C_m of samples slightly increase due to the activation of the active material, and then gradually decreased and finally tend to stable attributed to the degradation of active material to some extent at KOH electrolyte during subsequent GCD processes [34]. After 1000 cycles, the NiS electrode exhibits a relatively high C_m, demonstrating the microflower structure can act as buffer for the volume change in GCD process as well as convenient ion diffusion channels [54]. In addition, the GCD curves of the last 20 cycles of NiS electrode are shown as the Fig. 4H. Obviously, the GCD curves reveal a good symmetry and reproducibility, further confirming the superior redox reversibility.

The CV curves of NiS before and after 1000 GCD cycles at scan rate of 5 $mV \cdot s^{-1}$ are displayed in Fig. 5A. As shown in Fig. 5A, the CV curves are almost coincident, indicating the high stability of the NiS electrode. Fig. 5B, the Nyquist plots before and after 1000 GCD cycles, show obviously that the R_s values were increased from 0.22 Ω to 0.24 Ω, meanwhile, the value of R_{ct} increased from 2.99 Ω to 4.24 Ω. Moreover, the slight decrease of the slope for the straight line after 1000 GCD cycles. These results further confirm the highly cycling stability and good reversible redox reaction of the NiS. Fig. 5C and 5D show the SEM images of NiS before and after 1000 GCD tests. In comparison Fig. 5C with 5D, the NiS nanosheets become bent after cycling test. Such good stability of NiS is possibly attributed to the nanosheet structure, which can act as buffer for the volume shrinking and expanding during consecutive GCD process. Fig. S4 shows the XRD patterns of NiS electrodes before and after 1000 GCD cycles. It shows that the crystallinity degree slight decreased after GCD cycles. This phenomenon maybe from the fact that the consecutive GCD process makes volume of NiS electrode shrinkage and expansion constantly, leading to the crystallinity degree reduced. The evolution in crystallinity corresponds to the results of Fig. 5C and 5D.

As illustrated in Fig. 6A, the potential window of NiS electrode is within -0.1~0.6 V, while AC electrode within -0.1~0 V at scan rate of 5 $mV \cdot s^{-1}$. Moreover, the potential window of Ni//AC could be extended to 1.8 V, which is favorable for improving its energy density (Fig. 6B and 6C). Fig. 6B shows the CV curves of Ni//AC at different scan rate. The redox peak could be explicitly observed, attributing

to NiS pseudocapacitance. With the scan rate increasing from 5 $mV \cdot s^{-1}$ to 100 $mV \cdot s^{-1}$, the shape of CV curves has not obvious distortion, indicating fast charge/discharge property for Ni//AC [34]. Furthermore, from Fig. 6C, the GCD curves of Ni//AC are different from that of linear characteristic of EDLCs, indicating coexistence accumulation of electrostatic and redox reaction at electrode/electrolyte interfaces. Meanwhile, the GCD curves at different current densities are almost symmetric, demonstrating the excellent capacitance behavior. The C_m based on discharge curves at different current densities is calculated, displayed in Fig. 6D. The NiS//AC shows a C_m of 69.1, 57.7, 51.6, 44.9 and 30.2 $F \cdot g^{-1}$ at different current densities of 1, 2, 3, 5 and 10 $A \cdot g^{-1}$. The C_m at 10 $A \cdot g^{-1}$ still remained about 48.8% of that at 1 $A \cdot g^{-1}$, suggesting NiS//AC good rate capability.

Ragone plot for NiS//AC is shown in Fig. 6E. The energy density and power density were calculated according to the following equation:

$$E = C_m \times (\Delta V)^2 / 7.2 \qquad (5)$$

$$P = 3.6 \times E / \Delta t \qquad (6)$$

Where E is the energy density ($Wh \cdot kg^{-1}$), C_m is the specific capacitance ($F \cdot g^{-1}$), ΔV is the potential window for the discharge (V), P is the power density ($kW \cdot kg^{-1}$) and Δt is the discharge time (s). The NiS//AC can deliver an energy density of 31 $Wh \cdot kg^{-1}$ at a power density of 0.9 $kW \cdot kg^{-1}$ and still remain 12.9 $Wh \cdot kg^{-1}$ at power density of 8.8 $kW \cdot kg^{-1}$. As is generally known, the wide potential window of NiS//AC is a critical factor to improve the energy density.

The cycle life of the NiS//AC was evaluated by repeating GCD test for 1000

cycles at a current density of 5 $A \cdot g^{-1}$, as depicted in Fig. 6F. With the increase of cycle number, the C_m of NiS//AC increased first, and then tend to be stable. After 1000 cycles, the NiS//AC still retains 114.1% of its initial C_m. This indicates long–term cycle life of NiS//AC. Furthermore, the NiS//AC maintains a highly electrochemical reversibility with nearly 100% Coulombic efficiency after 1000 GCD cycles. The above-mentioned results reveal that the NiS//AC has superior capacitive performance due to NiS with large specific surface area, which are expected to improve the wettability of electroactive materials for enhancing the density of active sites.

4. Conclusions

In conclusion, the hierarchical NiS microflowers with superior capacitive performance were obtained through a facile two-step method. The NiS not only provide large specific surface area (26.3 $m^2 \cdot g^{-1}$), but also have a rough surface, which improve the active material/electrolyte contact area, shorten the diffusion pathway for ions. Electrochemical measurements results show that as-prepared NiS exhibited a high C_m (1122.7 $F \cdot g^{-1}$ at 1 $A \cdot g^{-1}$), low R_s (0.18 Ω) and R_{ct} (2.99 Ω), optimal rate capability and long cycle life (97.8% retention of C_m at 10 $A \cdot g^{-1}$ after 1000 cycles). Additionally, the NiS//AC, NiS as the positive electrode and AC as the negative electrode, has an operating voltage up to 1.8 V in 3 M KOH electrolyte, and delivers an energy density of 31 $Wh \cdot kg^{-1}$ at a power density of 0.9 $kW \cdot kg^{-1}$. In addition, the NiS//AC exhibits good electrochemical stability: the C_m retention is 114.1% at 5 $A \cdot g^{-1}$ and Coulombic efficiency after 1000 cycles retains nearly 100%. All above results signifies that NiS microflowers possess excellent capacitive performance, making it

highly promising electrode materials for SCs.

Acknowledgements

This work was financially supported by the Natural Science Foundation of China (NO. 21106124 and NO. 21375116) and Postdoctoral Science Foundation of China (2014M551668). The related measure and analysis instrument for this work was supported by the Testing Center of Yangzhou University.

5. References

[1] B. Li, M.B. Zheng, H.G. Xue, H. Pang, High performance electrochemical capacitor materials focusing on nickel based materials, Inorg. Chem. Front. 3 (2016) 175-202.

[2] J.H. Tang, J.F. Shen, N. Li, M.X. Ye, Facile systhesis of layered $MnWO_4$/reduced graphene oxide for supercapacitor application, J. Alloys Compounds 666 (2016) 15-22.

[3] P.F. Zhang, M. Chen, X. Shen, Q.H. Wu, X. Zhang, L. Huan, Preparation of $Li_4Ti_5O_{12}$ nanosheets/carbon nanotubes composites and application of anode materials for lithium-ion batteries, Electrochim. Acta 204 (2016) 92-99.

[4] Z.C. Li, J. Han, L. Fan, R. Guo, In-situ controllable growth of α-$Ni(OH)_2$ with different morphologies on reduced graphene oxide sheets and capacitive performance for supercapacitors, Colloid Polym. Sci. 294 (2016) 681-689.

[5] Z.C. Li, J. Han, L. Fan, M.G. Wang, S.Y. Tao, R. Guo, The anion exchange strategy towards mesoporous α-$Ni(OH)_2$ nanowires with multinanocavities for high-performance supercapacitors, Chem. Commun. 51 (2015) 3053-3056.

[6] R. Ding, M.Y. Zhang, Y.H. Yao, H. Gao, Crystalline $NiCo_2S_4$ nanotube array coated with amorphous $NiCo_xS_y$ for supercapacitor electrodes, J. Colloid Interface Sci. 467 (2016) 140-147.

[7] J.H. Wu, C.B. Ouyang, S. Dou, S.Y. Wang, Hybrid NiS/CoO mesoporous nanosheet arrays on Ni foam for high-rate supercapacitors, Nanotechnology 26 (2015) 325401.

[8] S.J. Peng, L.L. Li, H.T. Tan, R. Cai, W.H. Shi, C.C. Li, S. Mhaisalkar, M. Srinivasan, S. Ramakrishna, Q.Y. Yan, MS_2 (M=Co and Ni) hollow spheres with tunable interiors for high-performance supercapacitors and photovoltaics, Adv. Funct. Mater. 24 (2014) 2155-2162.

[9] Y. Zuo, J.J. Ni, J.M. Song, H.L. Niu, C.J. Mao, S.Y. Zhang, Y.H. Shen, Synthesis of Co_3O_4/NiO nanofilms and their enhanced electrochemical performance for supercapacitor application, Appl. Surf. Sci. 370 (2016) 528-535.

[10] Y.L. Zhang, L. Si, B. Zhou, B. Zhao, Y.Y. Zhu, L.H. Zhu, X.Q. Jiang, Synthesis of novel graphene oxide/pristine graphene/polyaniline ternary composites and application to supercapacitor, Chem. Eng. J. 288 (2016) 689-700.

[11] T. Peng, Z.Y. Qian, J. Wang, D.L. Song, J.Y. Liu, Q. Liu, P. Wang, Construction of mass-controllable mesoporous $NiCo_2S_4$ electrodes for high performance supercapacitors, J. Mater. Chem. A 2 (2014) 19376-19382.

[12] Y.Y. Wang, Y. Lei, J. Li, L. Gu, H.Y. Yuan, D. Xiao, Synthesis of 3D-nanonet hollow structured Co_3O_4 for high capacity supercapacitor, ACS Appl. Mater. Interfaces 6 (2014) 6739-6747.

[13] Q. Li, Z.L. Wang, G.R. Li, R. Guo, L.X. Ding, Y.X. Tong, Design and synthesis of MnO_2/Mn/MnO_2 sandwich-structured nanotube arrays with high supercapacitive performance for electrochemical energy storage, Nano Lett. 12 (2012) 3803-3807.

[14] V. Subramanian, H.W. Zhu, R. Vajtai, P.M. Ajayan, B.Q. Wei, Hydrothermal synthesis and pseudocapacitance properties of MnO_2 nanostructures, J. Phys. Chem. B 109 (2005) 20207-20214.

[15] K.B. Xu, R.J. Zou, W.Y. Li, Q. Liu, T. Wang, J.M. Yang, Z.G. Chen, J.Q. Hu, Carbon-coated mesoporous NiO nanoparticles as an electrode material for high performance electrochemical capacitors, New J. Chem. 37 (2013) 4031-4036.

[16] Z.M. Xu, A. Younis, D.W. Chu, Z.M. Ao, H.L. Xu, S. Li, Electrodeposition of mesoporous Co3O4 nanosheets on carbon foan for high performance supercapacitors, J. Nanomater. (2014) 902730.

[17] F. Li, G. Li, H. Chen, J.Q. Jia, F. Dong, Y.B. Hu, Z.G. Shang, Y.X. Zhang, Morphology and crystallinity-controlled synthesis of manganese cobalt oxide/manganese dioxides hierarchical nanostructures for high-performance supercapacitors, J. Power Sources 296 (2015) 86-91.

[18] Y.J. Wu, G.H. Gao, G.M. Wu, Self-assembled three-dimensional hierarchical porous V2O5/grapheme hybrid aerogels for supercapacitors with high energy density and long cycle life, J. Mater. Chem. A 3 (2015) 1828-1832.

[19] J.T. Zhang, X.S. Zhao, On the configuration of supercapacitors for maximizing electrochemical performance, ChemSusChem 5 (2012) 818-841.

[20] L.Y. Pei, Y. Yang, H. Chu, J.F. Shen, M.X. Ye, Self-assembled flower-like FeS_2/graphene aerogel composite with enhanced electrochemical properties, Ceram. Int. 42 (2016) 5053-5061.

[21] K.J. Huang, J.Z. Zhang, Y.L. Jia, K. Xing, Y.M. Liu, Acetylene black incorporated layered copper sulfide nanosheets for high-performance supercapacitor, J. Alloys Compounds 641 (2015) 119-126.

[22] Q.H. Liu, J. Huo, Z.L. Ma, Z.J. Wu, S.Y. Wang, In-situ formation of Ni_3S_2 interlayer between MoS_2 and Ni foam for high-rate and highly-durable lithium ion batteries, Electrochim. Acta 206 (2016) 52-60.

[23] X. Xu, D.M. Yu, H. Zhou, L. Zhang, C.H. Xiao, C.W. Guo, S.W. Guo, S.J. Ding, MoS_2 nanosheets grown on amorphous carbon nanotubes for sodium storage, J. Mater. Chem. A 4 (2016) 4375-4379.

[24] X. Xu, Z.Y. Fan, S.J. Ding, D.M. Yu, Y.P. Du, Fabrication of MoS_2 nanosheet@TiO_2 nanotube hybrid nanostructures for lithium storage, Nanoscale 6 (2014) 5245-5250.

[25] X. Xu, Z.Y. Fan, X.Y. Yu, S.J. Ding, D.M. Yu, X.W. Lou, A nanosheets-on channel architecture constructured form MoS2 and CMK-3 for high-capacity and long –cycle-life lithium storage, Adv. Energy Mater. (2014) 1400902.

[26] E.G.D.S. Firmiano, A.C. Rabelo, C.J. Dalmaschio, A.N. Pinheiro, E.C. Pereira, W.H. Schreiner, E.R. Leite, Supercapacitor electrodes obtained by directly bonding 2D MoS_2 on reduced graphene oxide, Adv. Energy Mater. 4 (2014) 1301380.

441 [27] X.F. Li, J.F. Shen, N. Li, M.X. Ye, Template-free solvothermal synthesis of NiS_2
442 microspheres on graphene sheets for high-performance supercaapacitors, Mater.
443 Lett. 139 (2015) 81-85.
444 [28] J.C. Xing, Y.L. Zhu, Q.W. Zhou, X.D. Zheng, Q.J. Jiao, Fabrication and shape
445 evolution of CoS_2 octahedrons for application in supercapacitors, Electrochim.
446 Acta 136 (2014) 550-556.
447 [29] H. Jiang, T. Sun, C.Z. Li, J. Ma, Hierarchical porous nanostructures assembled
448 from ultrathin MnO_2 nanoflakes with enhanced supercapacitive performances, J.
449 Mater. Chem. 22 (2012) 2751-2756.
450 [30] X.X. He, M.Y. Yang, P. Ni, Y. Li, Z.H. Liu, Rapid synthesis of hollow structured
451 MnO_2 microspheres and their capacitance, Colloids and Surfaces A: Physicochem.
452 Eng. Aspects 363 (2010) 64-70.
453 [31] J. Yan, T. Wei, J. Cheng, Z.J. Fan, M.L. Zhang, Preparation and electrochemical
454 properties of lamellar MnO_2 for supercapacitors, Mater. Res. Bull. 45 (2010)
455 210-215.
456 [32] H. Jiang, T. Zhang, J. Ma, C.Y. Yan, C.Z. Li, Ultrafine manganese dioxide
457 nanowire network for high-performance supercapacitors, Chem. Commum. 47
458 (2011) 1264-1266.
459 [33] J.X. Zhu, W.H. Shi, N. Xiao, X.H. Rui, H.T. Tan, X.H. Lu, H.H. Hng, J. Ma, Q.Y.
460 Yan, Oxidation-etching preparation of MnO_2 tubular nanostructures for
461 high-performance supercapacitors, ACS Appl. Mater. Interfaces 4 (2012)
462 2769-2774.

[34] H.H. Zhang, B. Guan, J.N. Gu, Y. Li, C. Ma, J. Zhao, T.Y. Wang, C.J. Cheng, One-step synthesis of nickel cobalt sulphides particles: tuning the composition for high performance supercapacitors, RSC Adv. 6 (2016) 58916-58924.

[35] H.H. Chen, J.J. Jiang, L. Zhang, H.Z. Wan, T. Qi, D.D. Xia, Highly conductive $NiCo_2S_4$ urchin-like nanostructures for high-rate pseudocapacitors, Nanoscale 5 (2013) 8879-8883.

[36] J.Q. Yang, X.C. Duan, Q. Qin, W.J. Zheng, Solvothermal synthesis of hierarchical flower-like β-NiS with excellent electrochemical performance for supercapacitors, J. Mater. Chem. A 1 (2013) 7880-7884.

[37] Z.Y. Dai, X.X. Zang, J. Yang, C.C. Sun, W.L. Si, W. Huang, X.C. Dong, Template synthesis of shape-tailorable NiS_2 hollow prisms as high-performance supercapacitor materials, ACS Appl. Mater. Interfaces 7 (2015) 25396-25401.

[38] H.H. Huo, Y.Q. Zhao, C.L. Xu, 3D Ni_3S_2 nanosheet arrays supported on Ni foam for high-performance supercapacitor and nonenzymatic glucose detection, J. Mater. Chem. A 2 (2014) 15111-15117.

[39] Z.C. Li, J. Han, L. Fan, R. Guo, Template-free synthesis of Ni_7S_6 hollow spheres with mesoporous shells for high performance supercapacitors, CrystEngComm, 17 (2015) 1952-1958.

[40] Y.J. Li, K. Ye, K. Cheng, J.L. Yin, D.X. Cao, G.L. Wang, Electrodeposition of nickel sulfide on grapheme-covered make-up cotton as a flexible electrode material for high-performance supercapacitors, J. Power sources 274 (2015) 943-950.

[41] C.B. Ouyang, X. Wang, C. Wang, X.X. Zhang, J.H. Wu, Z.L. Ma, S. Dou, S.Y. Wang, Hierarchically porous Ni_3S_2 nanorod array foam as highly efficient electrocatalyst for hydrogen evolution reaction and oxygen evolution reaction, Electrochim. Acta 174 (2015) 297-301.

[42] J.C. Xing, Y.L. Zhu, Q.W. Zhou, X.D. Zheng, Q.J. Jiao, Fabrication and shape evolution of CoS_2 octahedrons for application in supercapacitors, Electrochim. Acta 136 (2014) 550-556.

[43] H. Chen, L.F. Hu, Y. Yan, R.C. Che, M. Chen, L.M. Wu, One-step fabrication of ultrathin porous nickel hydroxide-manganese dioxide hybrid nanosheets for supercapacitor electrodes with excellent capacitive performance, Adv. Energy Mater. 3 (2013) 1636-1646.

[44] T. Zhu, Z.Y. Wang, S.J. Ding, J.S. Chen, X.W. Lou, Hierarchical nickel sulfide hollow spheres for high performance supercapacitors, RSC Adv. 1 (2011) 397-400.

[45] L. Peng, X. Ji, H.Z. Wan, Y.J. Ruan, K. Xu, C. Chen, L. Miao, J.J. Jiang, Nickel sulfide nanoparticles synthesized by microwave-assited method as promising supercapacitor electrodes: an experimental and computational study, Electrochim. Acta, 182 (2015) 361-367.

[46] L. Yu, B. Yang, Q. Liu, J.Y. Liu, X. Wang, D.L. Song, J. Wang, X.Y. Jing, Interconnected NiS nanosheets supported by nickel foam: Soaking fabrication and supercapacitors application, J. Electroanal. Chem. 739 (2015) 156-163.

[47] S.C. Tang, S. Vongehr, Y.G. Wang, J. Cui, X.Y. Wang, X.K. Meng, Versatile

synthesis of high surface area multimetallic nanosponges allowing control over nanostructure and alloying for catalysis and SERS detection, J. Mater. Chem. A 2 (2014) 3648-3660.

[48] H. Pang, C.Z. Wei, X.X. Li, G.C. Li, Y.H. Ma, S.J. Li, J. Chen, J.S. Zhang, Microwave-assisted synthesis of NiS_2 nanostructures for supercapacitors and cocatalytic enhancing photocatalytic H_2 production, Sci. Rep. 4 (2014) 3577.

[49] X. Wang, C.Q. Yan, A. Sumboja, J. Yan, P.S. Lee, Achieving high rate performance in layered hydroxide supercapacitor electrodes, Adv. Energy Mater. 4 (2014) 1301240.

[50] J.L. Mohanan, I.U. Arachchige, S.L. Brock, Porous semiconductor chalcogenide aerogels, Science 307 (2005) 397-400.

[51] W. Xing, F. Li, Z.F. Yan, G.Q. Lu, Synthesis and electrochemical properties of mesoporous nickel oxide, J. Power Sources 134 (2004) 324-330.

[52] Q. Pan, J. Xie, T.J. Zhu, G.S. Cao, X.B. Zhao, S.C. Zhang, Reduced graphene oxide-induced recrystallization of NiS nanorods to nanosheets and the improved Na-storage properties, Inorg. Chem. 53 (2014) 3511-3518.

[53] Y.F. Zhang, C.C. Sun, H.Q. Su, W. Huang, X.C. Dong, N-doped carbon coated hollow $Ni_xCo_{9-X}S_8$ urchins for high performance supercapacitor, Nanoscale, 7 (2015) 3155-3163.

[54] D.C. Wang, W.B. Ni, H. Pang, Q.Y. Lu, Z.J. Huang, J.W. Zhao, Preparation of mesoporous NiO with a bimodal pore size distribution and application in electrochemical capacitors, Electrochim. Acta 55 (2010) 6830-6835.

Fig. 1. Synthesis of hierarchical NiS microflowers.

Fig. 2. (A) XRD patterns of precursor and NiS; (B) N_2 adsorption-desorption isotherm and (C) pore size distribution curve for NiS; (D) XPS survey spectra of NiS; (E) Ni 2p and (F) S 2p.

Fig. 3. SEM images of precursor (A, B) and NiS (C, D); TEM images of precursor (E, F) and NiS (G, H); (I) HRTEM image of NiS.

Fig. 4. Electrochemical performance of NiS: (A) CV curves at different scan rates, (B) GCD curves at different current densities; Electrochemical performance of NiS and precursor ($Ni(OH)_2$): (C) C_m at different current densities, (D) CV curves at scan rate of 5 $mV \cdot s^{-1}$, (E) the GCD curves at current density of 1 $A \cdot g^{-1}$, (F) Nyquist plots, inset shows the corresponding equivalent circuit, (G) Cycling life at 10 $A \cdot g^{-1}$; (H) The last 20 GCD cycles of NiS.

Fig. 5. (A) CV curves, (B) Nyquist plots and (C, D) SEM images of NiS electrode before and after 1000 cycles.

Fig. 6. (A) CV curves of NiS and AC electrodes at scan rate of 5 $mV \cdot s^{-1}$; electrochemical performance of Ni//AC: (B) CV curves at different scan rates, (C) GCD curves at different current densities, (D) Variation of C_m at different current densities, (E) Ragone plot and (F) Cycle life and Coulombic efficiency at current density of 5 $A \cdot g^{-1}$.

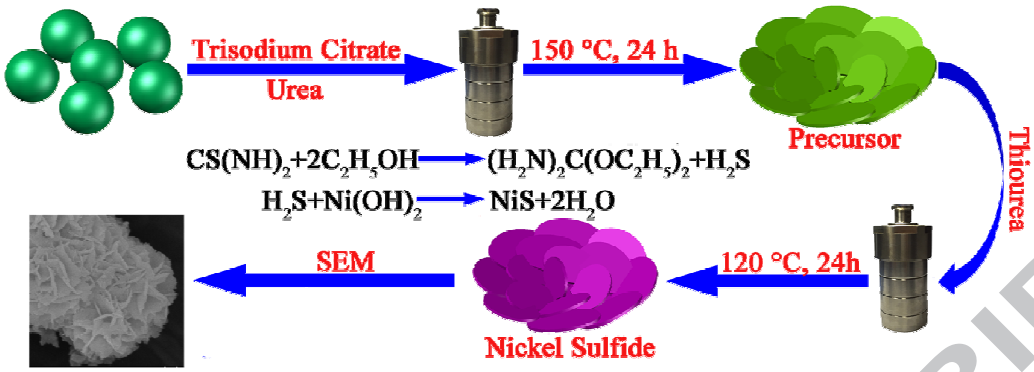

Fig. 1.

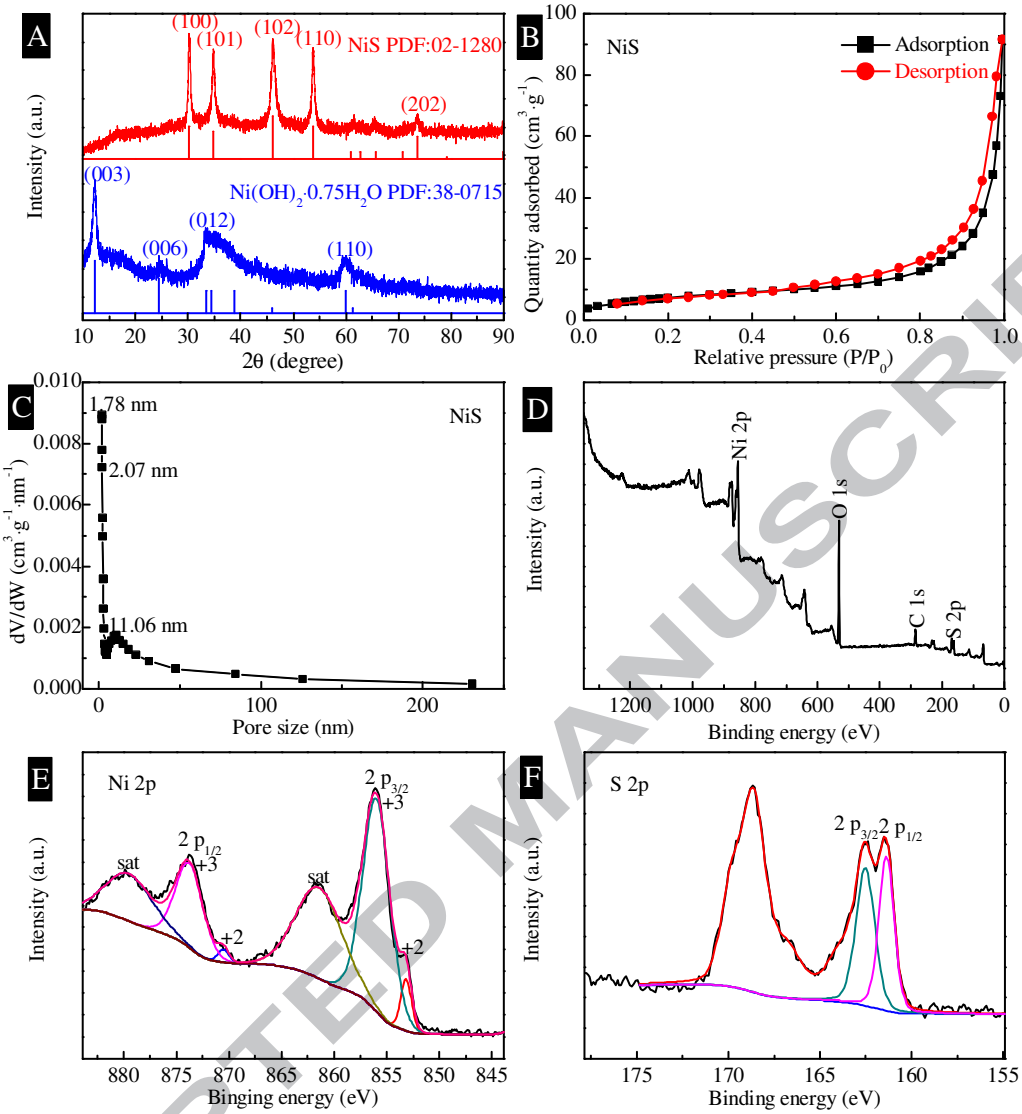

Fig. 2.

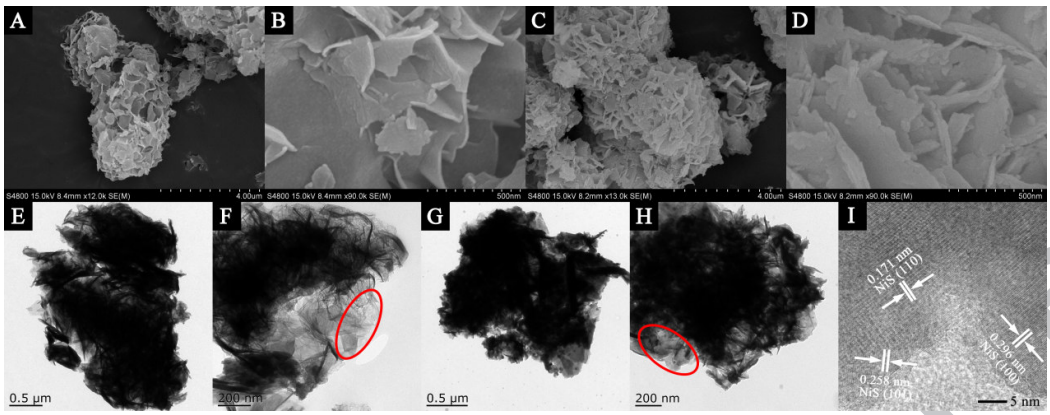

Fig. 3.

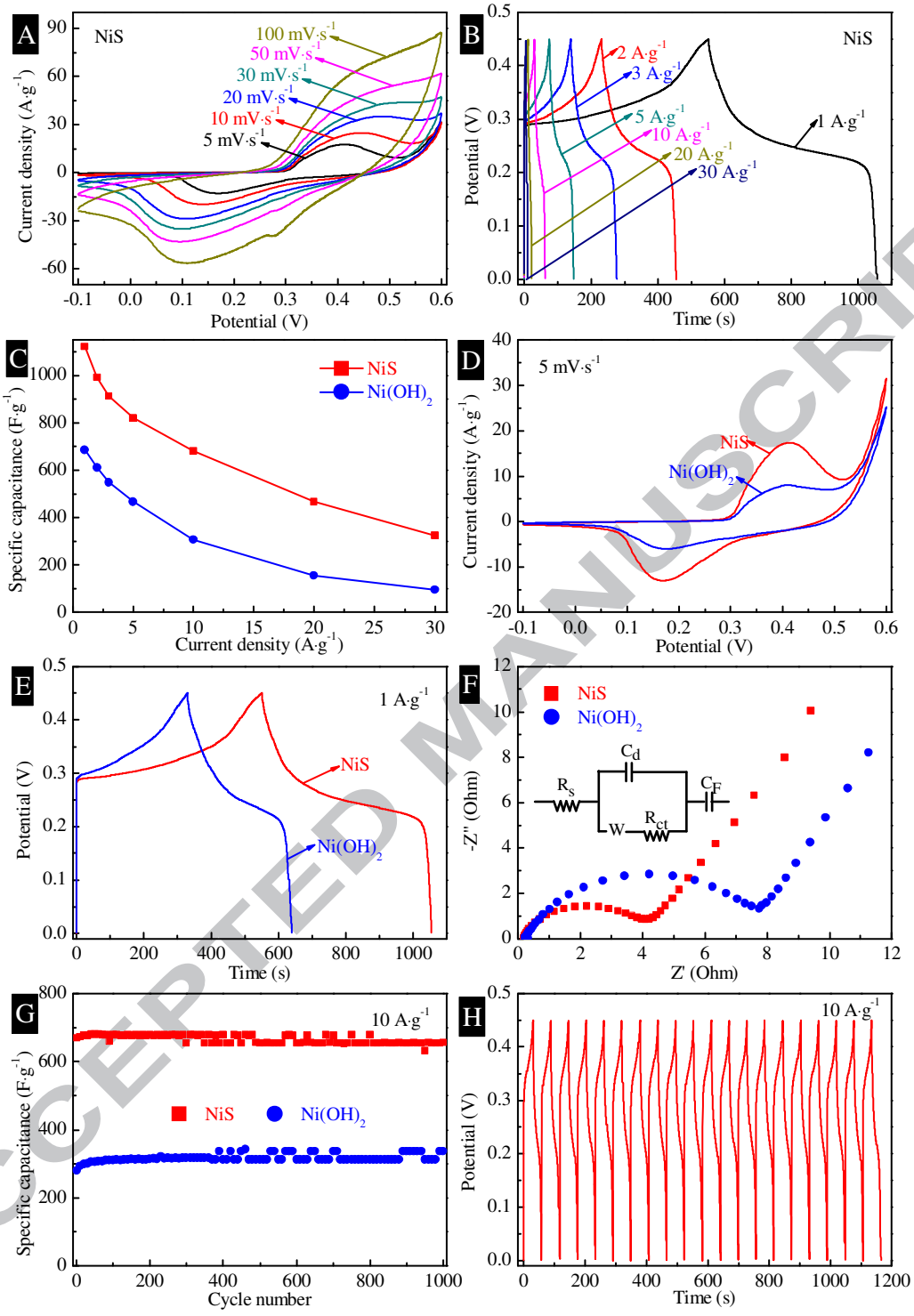

Fig. 4.

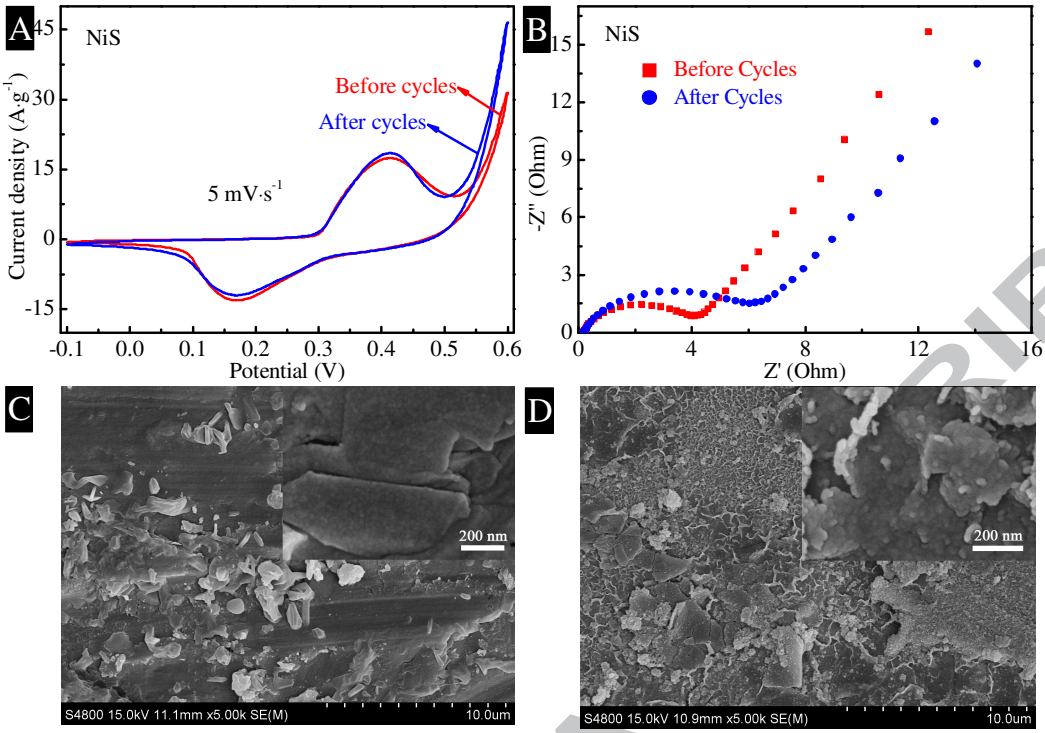

Fig. 5.

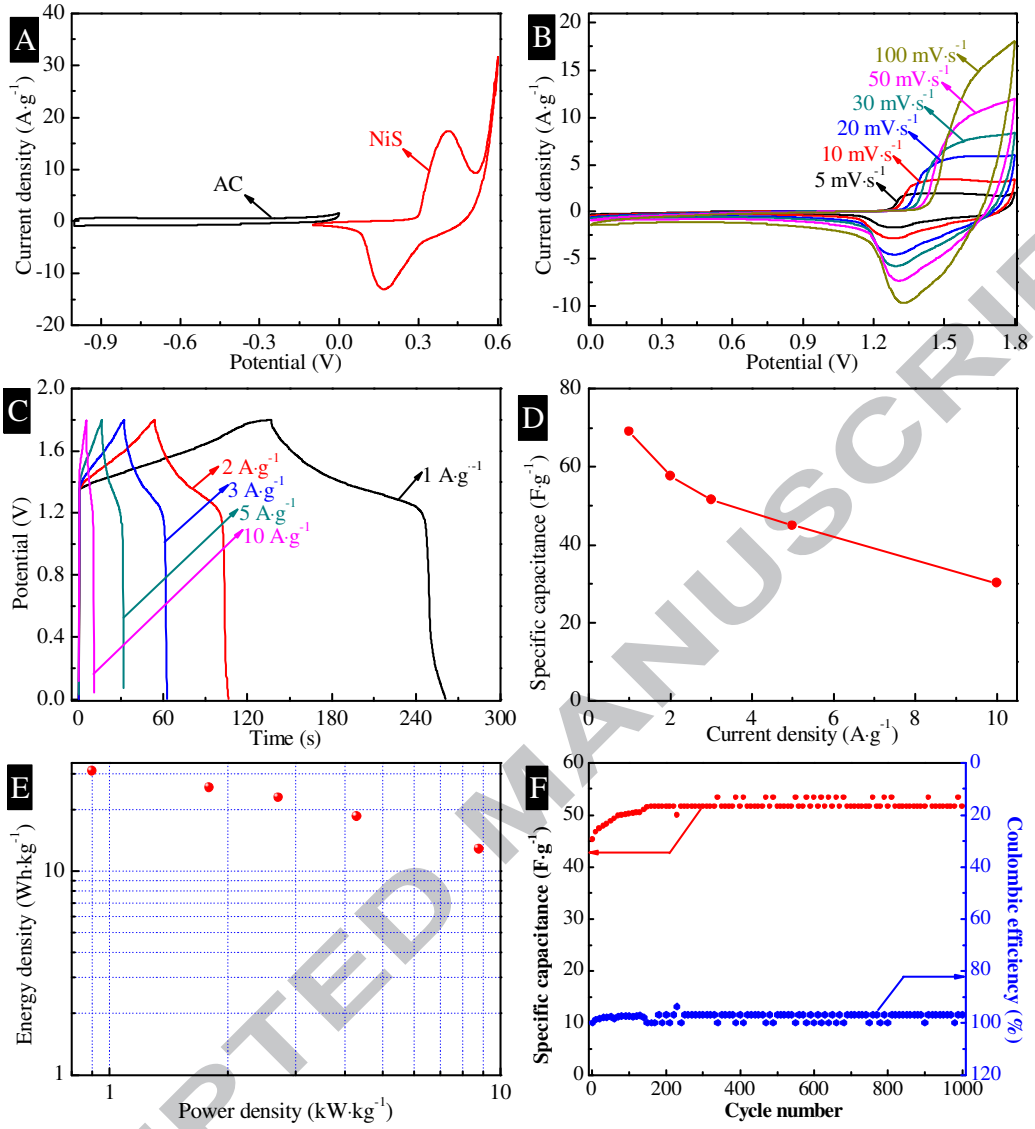

Fig. 6.

583 **Table 1** Comparison of the C_m of NiS electrodes with different forms from recent reports.

584

585

586

587

588 **Table 1**

Sample	Current density	Electrolyte	C_m ($F \cdot g^{-1}$)	Ref.
NiS microflower	1 $A \cdot g^{-1}$	3 M KOH	1122.7	This work
graphene nanosheets/NiS film	0.5 $A \cdot g^{-1}$	6 M KOH	775	40
NiS hollow spheres	4.08 $A \cdot g^{-1}$	2 M KOH	927	43
NiS nanoparticles	1 $A \cdot g^{-1}$	6 M KOH	845	45
NiS nanosheets	2.5 $mA \cdot cm^{-2}$	2 M KOH	527	46

589

590

591

592

593

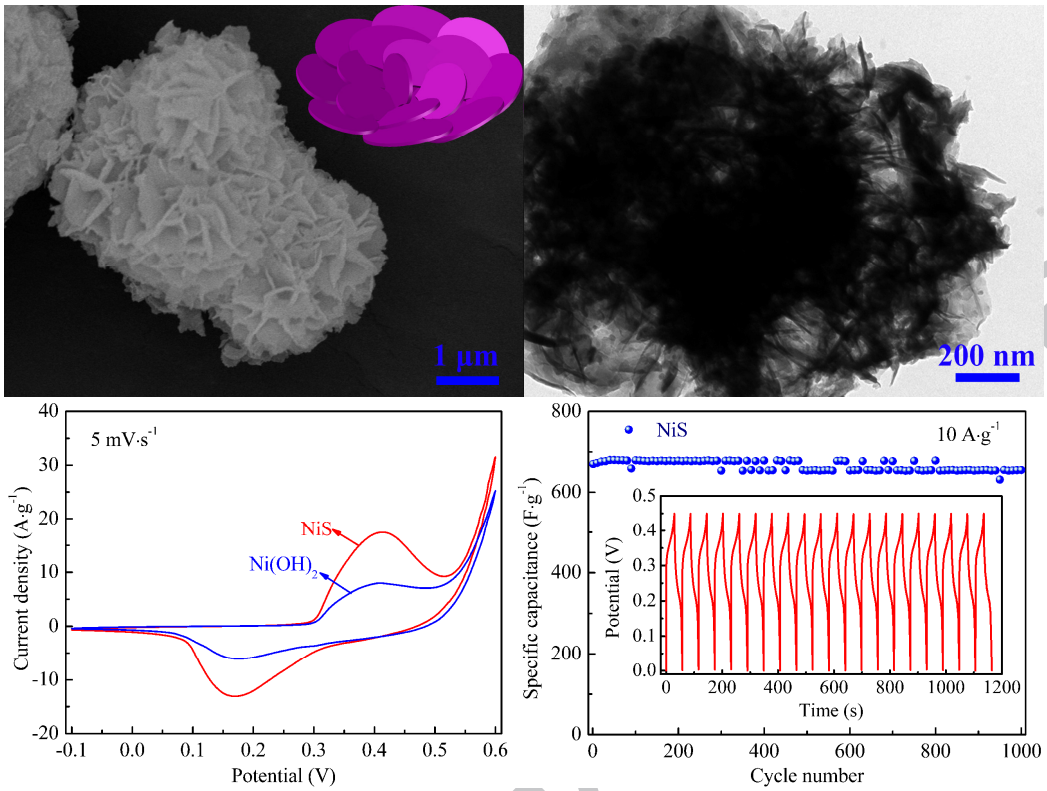

Hierarchical NiS microflowers were synthesized by a facile two-step method. Electrochemical measurements results show that the NiS owns the much high C_m and long cycle life.

Highlights

1. New hierarchical NiS microflowers with high capacitance performance were prepared.
2. Specific capacitance of NiS is up to 1122.7 $F \cdot g^{-1}$ at current density of 1 $A \cdot g^{-1}$.
3. Capacitance retention of NiS electrode after 1000 galvanostatic charge-discharge cycles is 97.8%.
4. NiS//AC delivers an energy density of 31 $Wh \cdot kg^{-1}$ at a power density of 0.9 $kW \cdot kg^{-1}$.